Defect Complexes in CrSBr Revealed Through Electron Microscopy and Deep Learning

Mads Weile,[1,2,*] Sergii Grytsiuk,[3] Aubrey Penn,[4] Daniel G. Chica,[5] Xavier Roy,[5] Kseniia Mosina,[6] Zdenek Sofer,[6] Jakob Schiøtz,[7] Stig Helveg,[2] Malte Rösner,[3] Frances M. Ross,[1,†] and Julian Klein[1,‡]

[1]*Department of Materials Science and Engineering, Massachusetts Institute of Technology, Cambridge, Massachusetts 02139, USA*

[2]*Center for Visualizing Catalytic Processes (VISION), Department of Physics, Technical University of Denmark, 2800 Kongens Lyngby, Denmark*

[3]*Institute for Molecules and Materials, Radboud University, Heijendaalseweg 135, 6525AJ Nijmegen, The Netherlands*

[4]*MIT.nano, Massachusetts Institute of Technology, Cambridge, Massachusetts 02139, USA*

[5]*Department of Chemistry, Columbia University, New York 10027, USA*

[6]*Department of Inorganic Chemistry, University of Chemistry and Technology Prague, Technická 5, 166 28 Prague 6, Czech Republic*

[7]*Department of Physics, Technical University of Denmark, DK-2800 Kongens Lyngby, Denmark*

(Received 9 September 2024; revised 18 December 2024; accepted 16 April 2025; published 4 June 2025)

Atomic defects underpin the properties of van der Waals materials, and their understanding is essential for advancing quantum and energy technologies. Scanning transmission electron microscopy is a powerful tool for defect identification in atomically thin materials, and extending it to multilayer and beam-sensitive materials would accelerate their exploration. Here, we establish a comprehensive defect library in a bilayer of the magnetic quasi-1D semiconductor CrSBr by combining atomic-resolution imaging, deep learning, and *ab initio* calculations. We apply a custom-developed machine learning work flow to detect, classify, and average point vacancy defects. This classification enables us to uncover several distinct Cr interstitial defect complexes, combined Cr and Br vacancy defect complexes, and lines of vacancy defects that extend over many unit cells. We show that their occurrence is in agreement with our computed structures and binding energy densities, reflecting the intriguing layer interlocked crystal structure of CrSBr. Our *ab initio* calculations show that the interstitial defect complexes give rise to highly localized electronic states. These states are of particular interest due to the reduced electronic dimensionality and magnetic properties of CrSBr and are, furthermore, predicted to be optically active. Our results broaden the scope of defect studies in challenging materials and reveal new defect types in bilayer CrSBr that can be extrapolated to the bulk and to over 20 materials belonging to the same FeOCl structural family.

DOI: 10.1103/PhysRevX.15.021080

Subject Areas: Condensed Matter Physics, Materials Science, Semiconductor Physics

I. INTRODUCTION

Atomic defects such as vacancies, dopants, or interstitials in two-dimensional (2D) van der Waals (vdW) materials have been studied extensively due to their ability to enhance the electronic, optical, magnetic, and chemical properties of the host material [1,2]. Atomic modifications, particularly through defect control, are essential for engineering quantum emitters [1], fabricating spintronic devices [3], or enhancing catalytic activity [4]. While defects have been studied in graphene [5], semiconducting transition metal dichalcogenides [6–8], and hexagonal boron nitride [9], achieving atomic-scale insight is more challenging in 2D magnets and other correlated materials due to poor air stability [10–14]. However, defects in these materials are particularly interesting considering their impact on the local magnetic and charge order as well as their potential role in quantum light emission.

An exciting host for defects is the vdW magnetic semiconductor CrSBr [15–17]. Bulk CrSBr exhibits a direct band gap of about 2 eV [18–20] and displays in-plane ferromagnetic and out-of-plane antiferromagnetic order [17,21]. The crystal structure of CrSBr is highly

*Contact author: weile.a.mads@gmail.com
†Contact author: fmross@mit.edu
‡Contact author: jpklein@mit.edu

Published by the American Physical Society under the terms of the Creative Commons Attribution 4.0 International license. Further distribution of this work must maintain attribution to the author(s) and the published article's title, journal citation, and DOI.

anisotropic, as seen in the material's quasi-1D electronic band structure that dominates quasiparticle physics [20] and charge transport [22]. Signatures of finite conductivity in low-temperature magnetotransport measurements [22,23] and spectrally narrow and magnetocorrelated photoluminescence emission [24] have been tentatively ascribed to originate from magnetic defects. To date, the defect types and quantities in CrSBr are not well characterized, and more detail is needed if we are to understand how defects alter magnetoelectronic properties or magnetic order [24–26]. The recently observed phenomenon of Cr atom mobility under exposure to high-energy electrons [27], as well as the use of helium ion irradiation [28] to modify magnetic order [25], motivate deliberate control of properties through defect control. In this case, too, knowledge of the (induced) defect structures is required to predict and design properties.

High-angle annular dark-field scanning transmission electron microscopy (HAADF-STEM) is a powerful tool that can assess atomic defects quantitatively in monolayer materials [5–7,9]. Low signal-to-noise ratios (SNRs) for detecting individual atomic defects is a challenge in such studies, but for defect analysis in monolayers the use of machine learning techniques, particularly deep convolutional neural networks (DCNNs), has become a widespread strategy to mitigate low SNR [29–33]. In bilayer or multilayer materials, the SNR of individual defects is even lower: Enabling similarly quantitative studies in thicker crystals would accelerate material exploration. Bilayer ($2L$) CrSBr, as a precursor model system for bulk CrSBr, is particularly compelling, as defects break structural, electronic, and magnetic symmetries to yield opportunities for optical emission [24]. Extending the application of DCNNs to thicker crystals would also be advantageous for the study of other beam-sensitive materials.

Here, we develop a STEM and deep learning approach that produces high-quality images of atomic defects and defect complexes in $2L$ CrSBr and quantifies defect types and frequencies. We achieve this by applying a custom-developed machine learning work flow to detect and classify single point vacancy defects while also extending to vertically stacked vacancy defects. Our statistical approach of obtaining averaged images with improved SNR reveals a surprising group of defect complexes that were not initially anticipated in the analysis. One of these is a combined Cr vacancy and Cr interstitial defect complex that exists in different variants and symmetries owing to the vdW gap geometry and interstitial energy landscape in CrSBr; another is a combined Cr and Br vacancy complex that is characteristic for this compound, where Br atoms share bonds with only two Cr atoms. Moreover, from the statistical distribution of Br vacancies, we also reveal extended defect lines of different length with an occurrence suggesting correlated formation behavior. We show *ab initio* density-functional theory (DFT) calculations of structures and binding energies that are in excellent agreement with our observations. In particular, the interstitial defect complexes exhibit strong electronic localization, and we suggest a range of quantum emission properties. Our study lays a foundation for utilizing the versatile group of defects that are evidently possible within CrSBr and can be extrapolated to many materials with the same FeOCl structural type. We conclude that the exceptional properties of CrSBr as a host for magneto-correlated and optically active defects, combined with its responsiveness to electron beam-induced structural transformation [27], suggest promising opportunities for controlled defect complex engineering.

II. METHODS

CrSBr is a ternary compound in which each layer consists of a network of Cr and S atoms encapsulated by Br atoms [see Fig. 1(a)]. It shows several important structural features. First, S and Br atoms reside in their own atom column distinct from the Cr atom column [see Fig. 1(a)]. Second, Br atoms are exclusively bonded to Cr atoms, forming a linear chain structure along the a direction. Third, due to the AA layer stacking order [34] with an interlayer distance of 7.965 Å [16], Br atom chains are displaced between adjacent layers to form interstitial sites between the layers and on the surface [see Fig. 1(a)] in both atom columns. This crystal structure, of the FeOCl type, is well known for intercalation [35]. The three features described above are important in understanding the types of defects in CrSBr we identify in this work.

We begin by describing our custom-built work flow for detecting defects in $2L$ CrSBr [see Fig. 1(b)]. For our material, $2L$ CrSBr, we focus on four different defect types: single V_{Br} and V_{Cr} vacancies in either of the layers, and vertically stacked bivacancies $V_{2\mathrm{Br}}^{\mathrm{bi}}$ and $V_{2\mathrm{Cr}}^{\mathrm{bi}}$ in both layers. We focus on defects related to Cr and Br because they lie within our detection sensitivity. We find that detecting V_S is challenging due to the low-Z contrast change, particularly in bilayers. This is in contrast to the assignment of Cr and Br related defects, as these exhibit distinguishable Z contrast.

For the machine learning work flow and training of our DCNNs, we simulate 600 HAADF-STEM images of 30×30 Å^2 flakes of CrSBr. These have been subjected to a variety of different transformations and noise sources to generalize the network to understand experimental data (see Supplemental Material [37]). Using the simulated images, a ground-truth label is constructed by centering Gaussians at each corresponding defect location with a standard deviation of $\sigma = 0.5$ Å. We find that realistic modeling of surface contamination is important to achieve robust results. We add fractal noise [38] to the simulated HAADF-STEM images (see Supplemental Material [37]) to enhance the effectiveness of our DCNNs to detect

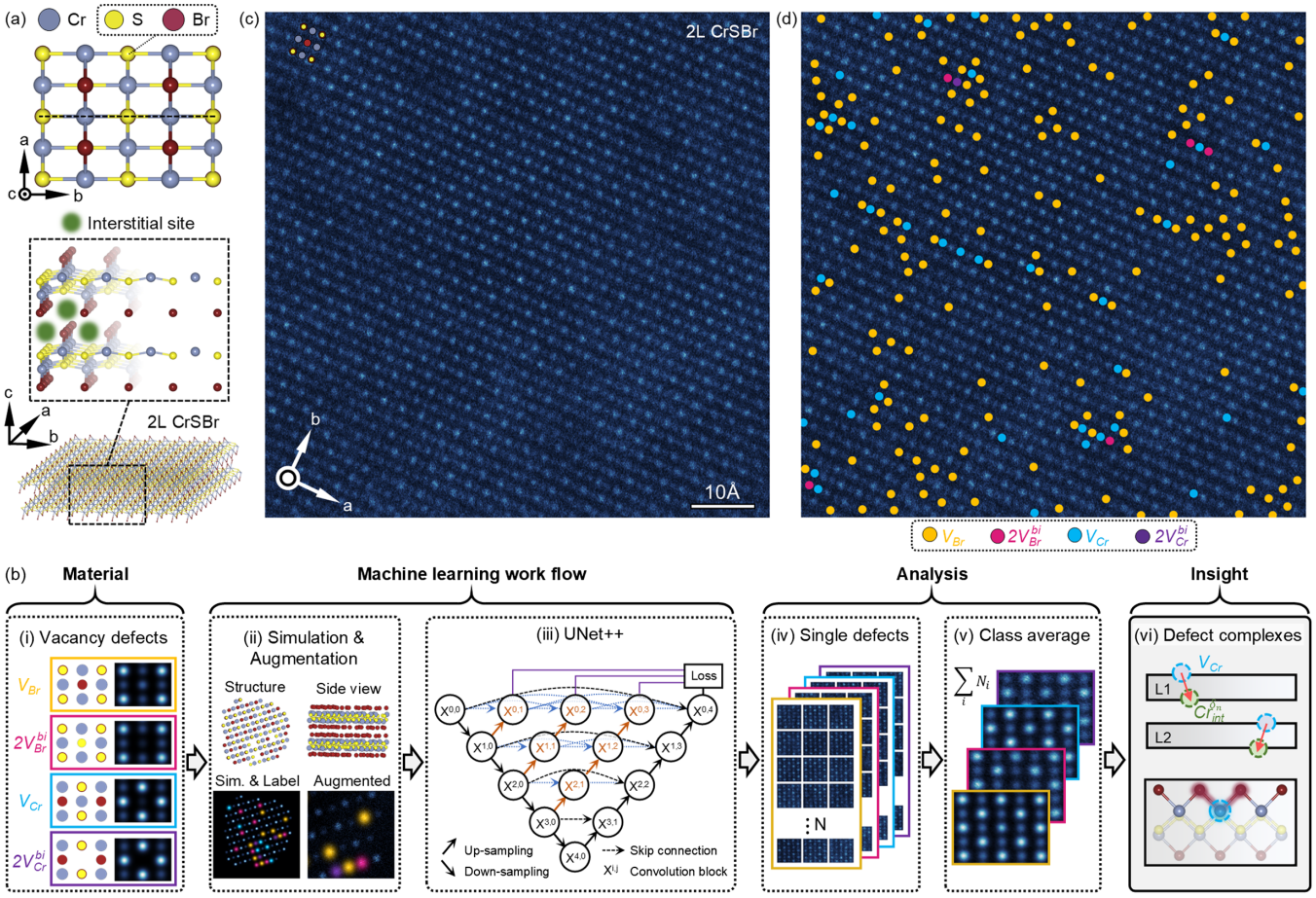


FIG. 1. Detecting vacancy defects in 2*L* CrSBr utilizing a custom-built machine learning work flow. (a) Crystal structure of 2*L* CrSBr and projected side view visualizing the atom stacking (S/Br on S/Br and Cr on Cr) in the *b*-*c* plane. (b) Step-by-step description of the work flow. (i) Four vacancy defects: V_{Cr} (blue), V_{Br} (purple), vertically stacked vacancies (in both layers) $V_{2\mathrm{Cr}}^{\mathrm{bi}}$ (orange), and $V_{2\mathrm{Br}}^{\mathrm{bi}}$ (pink), and their corresponding HAADF-STEM simulation. (ii) Image simulation and augmentation including vacancy defects and labeling. (iii) Neural network training using a UNet++ architecture [36]. (iv) DCNN output from experimental images showing individual detected defects. (v) Class averaging of classified vacancy defects to enhance SNR. (vi) Insights on defect complexes. (c) HAADF-STEM image of a 2*L* CrSBr using a beam current of 35 pA and energy of 200 keV. The total image dose is 9×10^6 $\mathrm{e}^-/\mathrm{nm}^2$. (d) Corresponding image with overlaid vacancy defects detected by DCNN.

defects in experimental images that exhibit this common type of contamination [39,40]. We expect that other imaging modalities, such as differential phase contrast imaging or ptychography, should be equally applicable for this work flow, particularly for light elements [41].

We employ two types of DCNNs: a defect network specialized in finding defects of interest and an atom-spotting network which is optimized for finding atomic positions (see Supplemental Material [37]) [42]. This allows the detection and subsequent alignment of defects with few-picometer precision. For both networks, we use the UNet++ architecture [36]. This architecture is a derivative of the classic UNet [43] and introduces additional pathways between the down- and up-sampling steps, effectively enabling an improved mapping across different length scales. The training process, parameters, and labeling are discussed in detail in Supplemental Material [37], and the code is also provided online [44].

We collect sequences of ten images of 2*L* CrSBr with a short dwell time (500 ns/px) that are averaged using rigid registration [45], resulting in a total dose of 9×10^6 $\mathrm{e}^-/\mathrm{nm}^2$ [see Fig. 1(c)]. Imaging is performed along the crystallographic *c* axis. The image shows the characteristic two columns with higher brightness for the S/Br atom column, where $Z(2\mathrm{S} + 2\mathrm{Br}) = 102$, and lower brightness for the Cr atom column, where $Z(2\mathrm{Cr}) = 48$, following the relationship between HAADF detector intensity and atomic number $I \sim Z^{1.6\text{–}1.7}$ [46]. Moreover, we observe defective regions that we ascribe to the material transfer process that exposes the material to solvents and low heat, in addition to defects that may occur from ambient humidity and from the electron beam during imaging (see Supplemental Material [37]).

We train an ensemble of four DCNNs and apply them to experimental HAADF-STEM images to predict vacancy defects. Figure 1(d) shows the HAADF-STEM image with overlaid predicted defects. Here, the most frequently detected defects are single vacancy defects, V_{Br} and V_{Cr}. Less frequently, we also observe the vertically stacked vacancies ($2V_{\mathrm{Br}}^{\mathrm{bi}}$ and $2V_{\mathrm{Cr}}^{\mathrm{bi}}$), typically in regions that appear more defective. Generally, the V_{Br} is the most abundant defect. The reduced stability of Br atoms is anticipated due to their position protruding from the layers. As halogens, Br atoms are particularly prone to surface chemical reactions, especially hydrolysis with water [28]. Our expectation also aligns with calculated defect binding energy densities (see Table I and Supplemental Material [37]). A high concentration of V_{Br} has also been observed in STM topographic images [24]. It is important to note that the densities we observe are substantially higher than the intrinsic defect concentration (see Supplemental Material [37]). We attribute this to the treatments required for sample preparation and the stability limitations of CrSBr (see Supplemental Material [37]).

III. RESULTS

After establishing the material problem and introducing our approach, we now apply our custom-built work flow to detect vacancy defects in a set of 13 experimental HAADF-STEM images with a total area of 832 nm^2 (see Supplemental Material [37]). A representative single image of V_{Br}, $2V_{\mathrm{Br}}^{\mathrm{bi}}$, V_{Cr}, and $2V_{\mathrm{Cr}}^{\mathrm{bi}}$ and their corresponding class averages are shown in Figs. 2(a) and 2(b), respectively. Obtaining statistical data on multiple images improves SNR, analogously to approaches used in cryo-electron microscopy [47]. Averaging is essential to analyze defects as the stability of $2L$ CrSBr allows for only low-dose imaging, resulting in low SNR. We compare the experimental images with simulations [see Fig. 2(c)] that are based on DFT-relaxed crystal structures. Line profiles taken along the b direction show excellent quantitative and qualitative agreement between experiment and simulation [see Fig. 2(d)]. The main disparity we observe is for the V_{Br}, where the central experimental intensity (arrowed) is higher than the simulated one. We attribute the discrepancy to the detection of false positives (identifying nondefects as defects). We note that the simulations should be treated as only a close approximation, as reproducing experimental conditions is difficult [48]. Under these challenging imaging conditions and low-Z contrast, both false positives and false negatives (failing to detect actual defects) can occur. However, by employing class averages, we minimize their impact: False positives result in less pronounced features in the averages, while false negatives do not contribute. Additionally, we further reduce false positives by applying a detection threshold of 0.95 for V_{Br} (which has the lowest

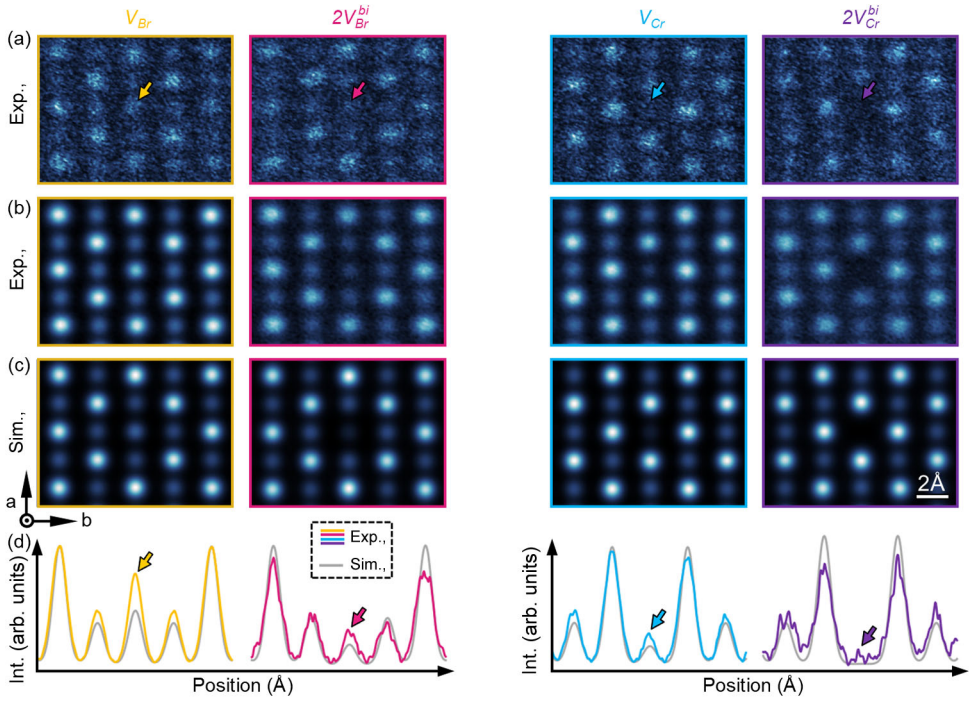


FIG. 2. Single and vertically stacked vacancy defects in $2L$ CrSBr. (a) Single HAADF-STEM images of four types of vacancies (V_{Br}, $2V_{\mathrm{Br}}^{\mathrm{bi}}$, V_{Cr}, and $2V_{\mathrm{Cr}}^{\mathrm{bi}}$) detected by DCNN. The image size is 11.93 Å by 8.75 Å. Arrows highlight the S/Br and Cr defect column, respectively. (b) Corresponding class-averaged images with a total of $N = 1242$, 64, 264, and 36 images per vacancy defect. (c) Corresponding simulated HAADF-STEM images from DFT-relaxed crystal structures, performed using the experimental imaging parameters. (d) Comparison between experimental and simulated intensity line profiles from (b) and (c) along the b direction.

contrast change, compared to its pristine counterpart) and 0.90 for all other defects. As well as calculating class averages, we also verify that our trained networks provide statistically significant outputs by performing two additional cross-validation approaches (see Supplemental Material [37]).

The statistical approach using deep learning combined with the quantitative nature of collecting HAADF-STEM images equips us with the ability to spot not only the presence of vacancy sites, but potentially more intricate defects that either involve multisite vacancy complexes or atoms residing in proximal atom columns as interstitials. The latter are particularly relevant for CrSBr, considering the mobility of Cr atoms when exposed to high-energy electrons [27].

With this in mind, we revisit atom column intensities of the first- and second-nearest-neighbor (NN) S/Br and Cr atom columns in the class-averaged V_{Cr} [see Fig. 3(a)] and create a corresponding Voronoi diagram by integrating a circular mask around each atom [see Figs. 3(b) and 3(c)] [49]. Because the class average represents a statistical measurement across our 264 detected V_{Cr} related defects, we can treat it as a probabilistic measure to observe other more complex defect types. We note that this considers only defects that are connected to the occurrence of a nearby V_{Cr}. We make two striking observations. First, there

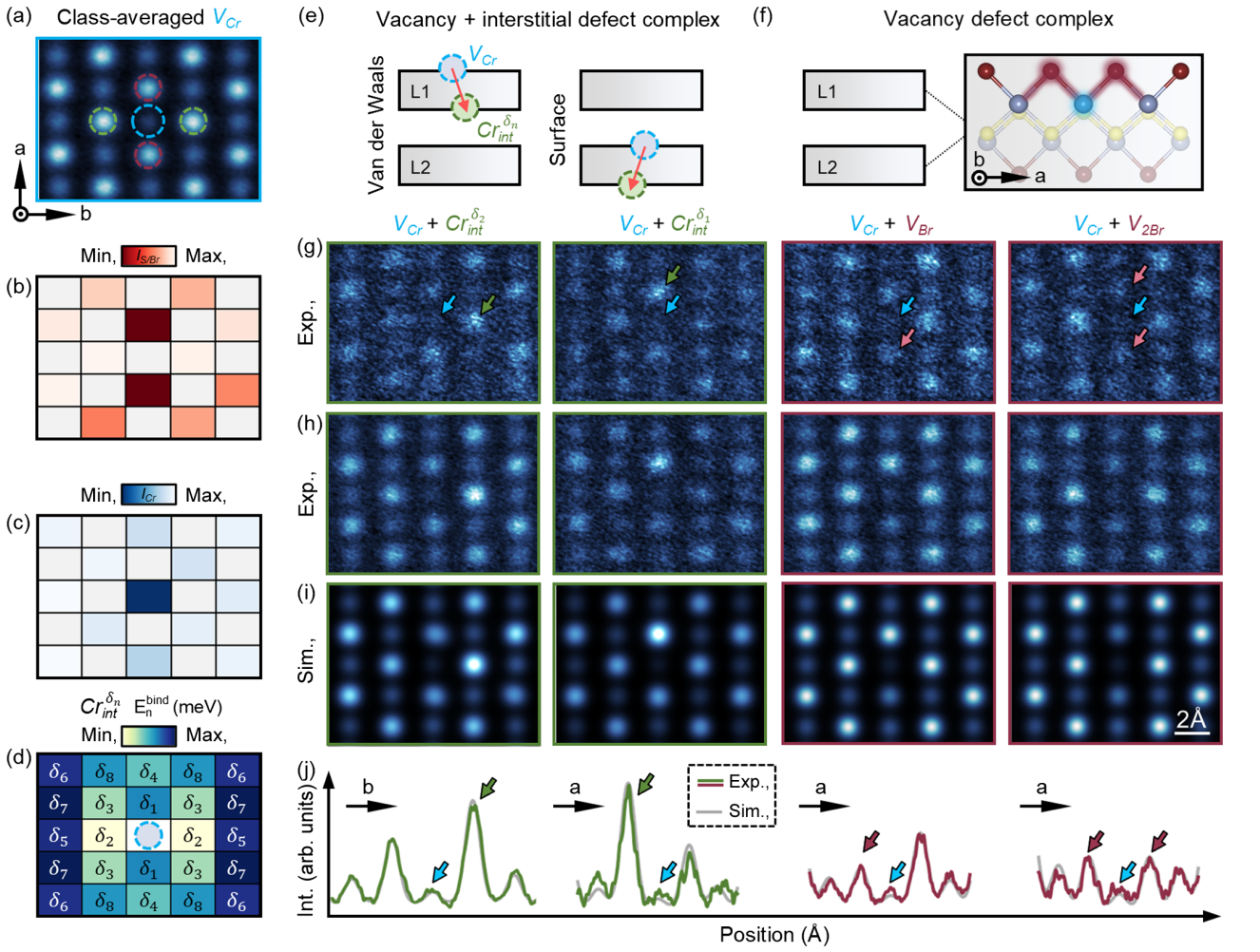


FIG. 3. Interstitial and vacancy defect complexes in 2L CrSBr. (a) Class-averaged HAADF-STEM image of V_{Cr} from Fig. 2(b). Nearest-neighbor (NN) S/Br atom columns along the a (red) and b direction (green) are highlighted. (b), (c) Corresponding Voronoi intensity diagram of the S/Br and Cr atom columns. (d) DFT calculated binding energy density of first- and second-NN Cr interstitial defects. (e) Vacancy-interstitial defect complex with Cr_i situated between layers ($L1$ and $L2$) in the van der Waals gap or at the surface. (f) Vacancy defect complex due to exclusive Cr–Br bond. (g) Single experimental HAADF-STEM images of vacancy-interstitial defect complexes $V_{\mathrm{Cr}} + \mathrm{Cr}_{\mathrm{int}}^{\delta 2}$ and $V_{\mathrm{Cr}} + \mathrm{Cr}_{\mathrm{int}}^{\delta 1}$ as well as $V_{\mathrm{Cr}} + V_{\mathrm{Br}}$ and $V_{\mathrm{Cr}} + V_{2\mathrm{Br}}$ defect complexes. (h) Corresponding class-averaged images with a total of $N = 11$, 3, 12, and 6 images per defect type. (i) Simulated images from DFT-relaxed crystal structures. (j) Comparison between experimental and theoretical intensity line profiles from (h) and (i) along the b direction or a direction.

is reduced intensity in the first-NN S/Br column along the a direction, and, second, there is increased intensity along the S/Br column along the b direction. We interpret these intensities through the presence of two categories of defect complexes. One is a V_{Cr} in combination with a Cr interstitial $Cr_{int}^{\delta n}$ with δn as the specific position of the Cr interstitial atom [see Fig. 3(e)], and the other is a vacancy complex consisting of V_{Cr} and one or two V_{Br} along the a direction [see Fig. 3(f)].

We first discuss the class of Cr interstitial defect complexes. Formation probabilities can be estimated based on *ab initio* DFT calculations. For this, we determine the binding energy density of eight Cr interstitial defects $V_{Cr} + Cr_{int}^{\delta n}$ with $n = 1$–8 representing the location of the interstitial [see Fig. 3(d), Table I, and Supplemental Material [37]]. This is calculated by $E_{Cr_{int}^{\delta n}}^{bind} = \{[E_N - (E_{N-Cr_{int}^{\delta n}} + E_{Cr_{int}^{\delta n}})]/(N_{cells})\}$, which is defined as the energy to remove the $Cr_{int}^{\delta n}$ atom from the unit cell consisting of N atoms. A lower E_n^{bind} suggests a higher probability of forming a Cr interstitial defect complex. We find the $V_{Cr} + Cr_{int}^{\delta 2}$ to be energetically most favorable. Importantly, in $2L$ CrSBr, and, more generally, in multilayer CrSBr, we need to distinguish further between a Cr interstitial that is situated between vdW layers and one at the surface [see Fig. 3(e)]. As may be expected, interstitials located in the vdW gap are calculated to be more stable compared to interstitials situated at the surface (see Table I and Supplemental Material [37]).

Manually searching through images of all detected V_{Cr} and locating increased intensity in first- and second-NN S/Br and Cr atom columns, we identify several prominent types of Cr interstitial defect complexes [see Figs. 3(g) and 3(h)]. Most common is the $V_{Cr} + Cr_{int}^{\delta 2}$ (Cr in the S/Br column along the b direction). Its relatively frequent occurrence is in excellent agreement with the lowest binding energy density $E_{\delta 2}^{bind} = 105$ meV [see Fig. 3(d)]. Moreover, we also observe interstitial defects with the Cr atom residing in the closest S/Br atom column along the a direction to form the $V_{Cr} + Cr_{int}^{\delta 1}$ complex ($E_{\delta 1}^{bind} = 149$ meV). It is unknown whether the observed interstitial is thermally or kinetically stable; however, a match with DFT calculations of lowest-energy motifs suggest that, irrespective of the formation mechanism, the observed features seem to be thermally equilibrated. Indeed, we also observe this type of relocation of Cr atoms during beam exposure in $2L$ CrSBr (see Supplemental Material [37]). We further note that it is unclear whether all observed interstitials are beam induced or formed during sample fabrication or material synthesis. The class averages show excellent agreement with simulated images of corresponding DFT-relaxed crystal structures [see Fig. 3(i)], as assessed by comparing line profiles along the b and a directions [see Fig. 3(j)]. We note that the different configurations and locations of the Cr interstitial (vdW and surface) create lattice distortions that result in qualitative differences in the simulated image intensities (see Supplemental Material [37]). While we have focused on the $V_{Cr} + Cr_{int}^{\delta 1}$ and $V_{Cr} + Cr_{int}^{\delta 2}$ interstitial defect complexes, other Cr interstitial defect complexes may also be formed under the electron beam.

We now discuss the vacancy complex consisting of V_{Cr} with V_{Br}. Using the same approach as in searching for Cr interstitials, we manually assess the V_{Cr} for an intensity reduction at the position indicated in Fig. 3(a) as suggested from our Voronoi diagram [see Fig. 3(b)]. We do indeed identify the presence of $V_{Cr} + V_{Br}$ and $V_{Cr} + 2V_{Br}$ vacancy defect complexes [see Figs. 3(g) and 3(h)]. The presence of such complexes is intuitive, as the Br atoms are exclusively bonded to the Cr atoms [see Fig. 3(f)], and the presence of V_{Cr} lowers E^{bind} of a Br atom from 350 to 306 meV for V_{Br} or to 293 meV for $2V_{Br}$ (see Table I and Supplemental Material [37]). Line profiles from the class-averaged images obtained from the manual search are in excellent agreement with simulated images from DFT-relaxed structures [see Figs. 3(i) and 3(j)]. Computationally searching through all V_{Cr} that show V_{Br} or $2V_{Br}$ in the first-NN S/Br columns, we find that V_{Cr} is concurrent with V_{Br} 43% of the time and V_{2Br} with 19%. This suggests the frequent formation of $V_{Cr} + V_{Br}$ and $V_{Cr} + V_{2Br}$ defect complexes, most likely at the surface of the bilayer. We note that purely based on HAADF-STEM images we are not able to distinguish whether the vacancy is the Br atom site at the surface or the one close to the vdW gap.

Considering the volatility of surface Br atoms and their arrangement in chains along the a direction, we now study their statistical distribution more closely to assess potential correlations based on their occurrence and spatial arrangement. To this end, we analyze and quantify both individual V_{Br} and extended V_{Br} defect chains along the a direction [see Fig. 4(a) and Supplemental Material [37]]. Interestingly, we find that the statistical distribution of Br vacancy defect lengths is best captured by a power-law distribution [see Fig. 4(a) and Supplemental Material [37]], suggesting that V_{Br} exhibit correlated, extended growth patterns. We observe that deviations from the expected power-law behavior may result from false positives or false negatives in the detection of Br defects. Specifically, false positives can lead to an increased number of detected individual V_{Br} defects, while false negatives can reduce the count of longer extended defect lines.

While a Br vacancy can initiate the formation of defect chains, a Cr vacancy is an even more likely nucleation site, as it significantly lowers the defect formation energy of the two neighboring Br atoms to which it is bonded. Indeed, in our class-averaged images of different defect lengths [see Fig. 4(b)], we see not only V_{Br}, but also V_{Cr} participate in forming extended 1D defect lines. The presence of either vacancy reduces the formation energy of adjacent defects. For example, once a V_{Cr} forms, the subsequent defect

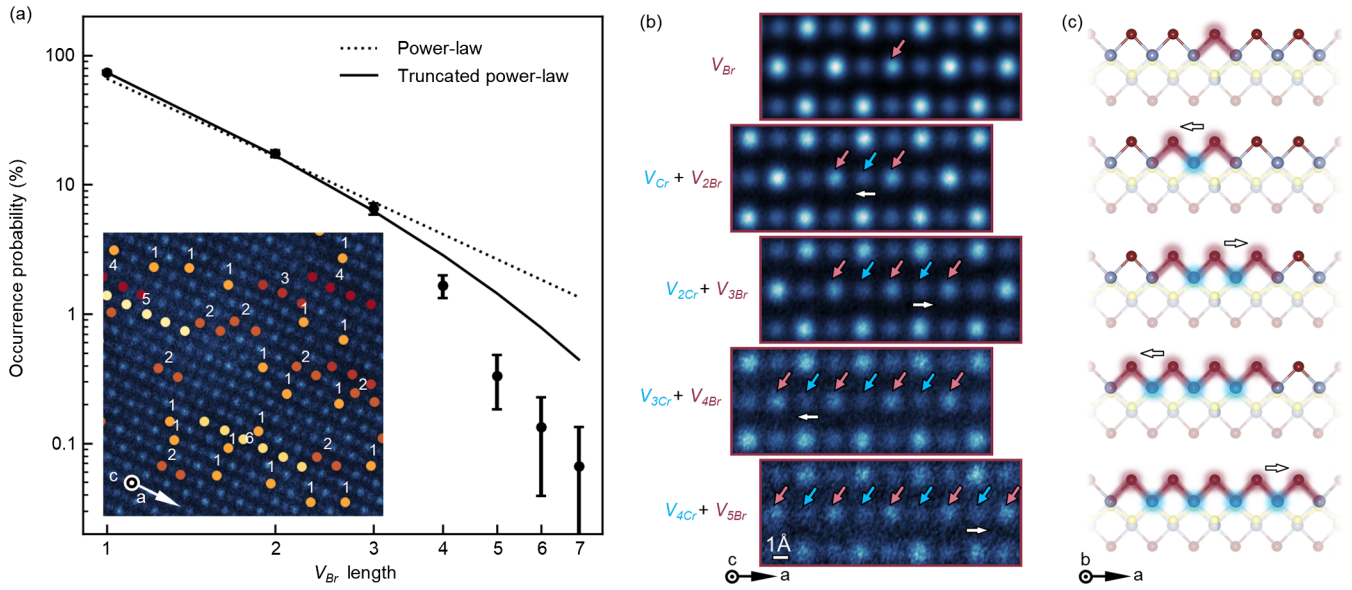


FIG. 4. Extended 1D line defects in 2L CrSBr. (a) Probability of defect chains of different lengths following a power-law dependence. Inset: HAADF-STEM image with detected Br vacancy defect lines of different lengths. (b) Class averages with a total of $N = 1109$, 262, 98, 25, and 5 images per defect length type. (c) Illustration of defect chain growth along the a direction.

formation energy for an adjacent V_{Br} decreases, which facilitates the formation of extended line defects [see Fig. 4(c) and Supplemental Material [37]]. As this mechanism repeats, long defective chains composed of missing Br and Cr atoms can develop along the a direction. Based on our electronic structure calculations (see Supplemental Material [37]), we anticipate the formation of various types of line defects. Among these, the pure V_{Br} defects, along with V_{Br} in conjunction with fewer V_{Cr} vacancies, are expected to represent the most energetically favorable configurations.

Several factors likely contribute to the correlated formation and extension of these defect lines. The relatively low formation energy of V_{Br} makes Br atoms particularly volatile. Mechanisms that can drive the growth of defect lines include surface reconstruction, strain relaxation, or external chemical influences, such as hydrolysis from H_2O or oxidation from O_2 [28]. Such reactions are particularly dominant on surface layers.

The identification and quantification of Br vacancy defects, defect complexes, and extended line defects are relevant for interpreting transport measurements on CrSBr [22,23]. Recent conductivity measurements reported an extreme anisotropy between the a and b directions with a strong gate voltage dependence [22]. Despite the characteristic flat conduction band along the a direction and a highly dispersive band along the b direction with an effective electron mass ratio of about 50 [20], the highest anisotropy is observed for hole doping but is suppressed for electron doping [22]. This unexpected response suggests that defects may be important for interpreting the transport measurements. Our calculations show that the most abundant type of defect, the V_{Br}, induces a shallow donorlike state close to the conduction band minimum (see Supplemental Material [37]), effectively n-doping CrSBr, as also observed in transport experiments [22,23]. Moreover, from our calculations of smaller supercells, we also see defect-line-induced dispersions along the a and b directions that could potentially promote hopping transport. In our study, we not only verify a high concentration of V_{Br}, but, more strikingly, also observe the formation of 1D defect lines ($V_{(n)\mathrm{Br}}$ and $V_{(n)\mathrm{Br}} + V_{(n-1)\mathrm{Cr}}$) with up to $n = 7$ Br atoms extending for more than 2 nm. To study their effect on the electronic band structure and, therefore, transport properties, we calculate infinite vacancy lines along the a direction (see Supplemental Material [37]). These calculations show dispersion and metallic behavior along the a but also the b direction. This suggests that defect lines not only contribute free electrons, increasing the intrinsic carrier concentration, but can likely also contribute to the gate-voltage-dependent conductivity anisotropy observed along the a and b directions.

These results imply that surface vacancy engineering and chemical manipulation can provide a means to control electronic transport properties in this material system, potentially enabling tunable anisotropic transport properties through deliberate defect engineering. This becomes particularly important for mono- and bilayer CrSBr flakes due to their high surface-to-volume ratio, but is also important for bulk material where it is expected that defects in surface layers contribute disproportionately to bulk device transport due to their higher density of interface states.

We can now discuss the magnetoelectronic footprints of the defects that are most frequently observed experimentally. We calculate the electronic structure by means of spin-resolved DFT + U calculations for 4×3 supercells of

$2L$ CrSBr. We are particularly interested in the coupled electronic and magnetic degrees of freedom of the defects, as CrSBr exhibits strongly magnetocorrelated physics [17,20,21,24,50]. Moreover, we are also interested in the magnetic coupling of the Cr interstitials, as they are expected to affect local magnetic intra- and interlayer ordering [24,25,27].

We calculate the electronic band structure of pristine [see Fig. 5(a)] and defective $2L$ CrSBr supercells [see Figs. 5(b)–5(d)] alongside their real-space defect charge densities. For the defective band structures, we consider the Cr vacancy defects V_{Cr} and $2V_{\mathrm{Cr}}^{\mathrm{bi}}$ [see Fig. 5(b)], the Cr interstitial vacancy complexes $V_{\mathrm{Cr}} + \mathrm{Cr}_{\mathrm{int}}^{\delta 2}$ and $V_{\mathrm{Cr}} + \mathrm{Cr}_{\mathrm{int}}^{\delta 1}$ [see Fig. 5(c)], and the Cr and Br vacancy complexes $V_{\mathrm{Cr}} + V_{\mathrm{Br}}$ and $V_{\mathrm{Cr}} + V_{2\mathrm{Br}}$ [see Fig. 5(d) and Supplemental Material [37]].

We note that in the LDA $+ U$ approximation the band gap of the pristine $2L$ CrSBr is underestimated. Otherwise, we find in Fig. 5(a) the expected characteristics such as highly anisotropic dispersions in the lowest conduction bands as well as the antiferromagnetic alignment between the ferromagnetic single layers, which combined with the inversion symmetry of the $2L$ system results in a fully spin-degenerate electronic structure. In all calculated defect structures, we find multiple weakly dispersive in-gap states, indicating the highly localized character of these impurity states in real space (which still hybridize here due to periodic boundary conditions and the finite size of the supercells).

In general, as illustrated in Fig. 5, the atoms surrounding the defects predominantly contribute to the impurity states near the Fermi level, exhibiting distinct orbital characters for various defects. Although the p orbital of sulfur atoms is present in all cases, the Cr d orbital significantly contributes only in the presence of Cr displacements ($V_{\mathrm{Cr}} + \mathrm{Cr}_{\mathrm{int}}^{\delta}$ defects). In structures with pure Cr vacancy defects, there is a notable contribution from the p orbital of Br atoms; however, this contribution nearly disappears when two Br atoms adjacent to the Cr vacancy are removed. Additionally, the contribution from the Br p orbitals is highly dependent on the displacement direction of the Cr atoms and the location of the resulting Cr vacancy, peaking for the δ_1 displacement and nearly vanishing for the δ_2 displacement.

In the case of the single Cr vacancy V_{Cr} depicted in Fig. 5(b), we find various defect in-gap states around the Fermi level with partially vanishing dispersion. Most importantly, we see that the impurity states inherit the spin state of the monolayer in which the defect is situated.

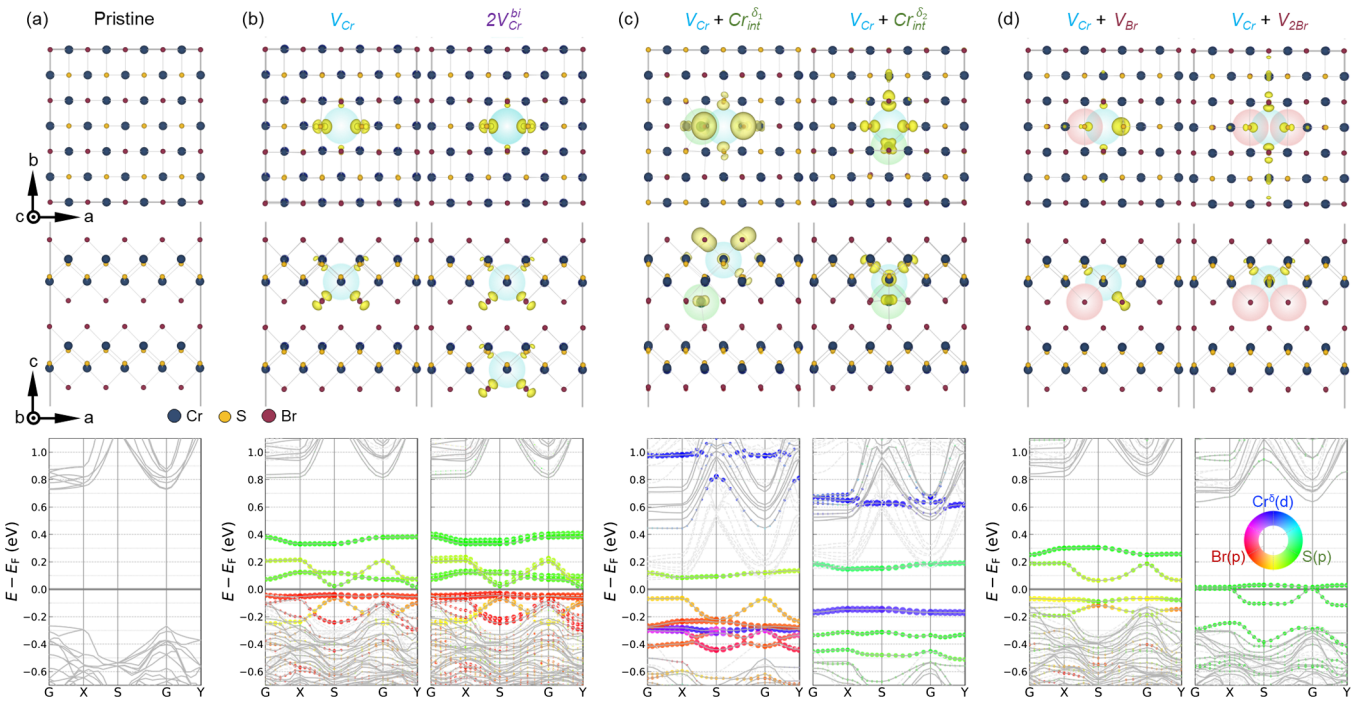


FIG. 5. Electronic structure of single defects and defect complexes in $2L$ CrSBr. Upper panels show the DFT $+ U$-relaxed crystal structures and defect wave functions for (a) the pristine $2L$ CrSBr 4×3 supercell, (b) single Cr vacancies (V_{Cr} and $V_{2\mathrm{Cr}}^{\mathrm{bi}}$), (c) interstitial defects ($V_{\mathrm{Cr}} + \mathrm{Cr}_{\mathrm{int}}^{\delta 1}$, $V_{\mathrm{Cr}} + \mathrm{Cr}_{\mathrm{int}}^{\delta 2}$), and (d) two vacancy complexes ($V_{\mathrm{Cr}} + V_{\mathrm{Br}}$ and $V_{\mathrm{Cr}} + V_{2\mathrm{Br}}$). The charge densities associated with defects are shown in yellow, while Cr and Br vacancies and Cr interstitial atoms are indicated by light blue, dark red, and green spheres, respectively. Lower panels show the electronic band structures for the same configurations. Colored bands represent defect-induced majority orbital wave function admixtures from Cr d orbitals and p orbitals of S and Br in the defect vicinity. Solid lines in gray denote the majority spin channel, while dashed lines indicate the minority spin channel.

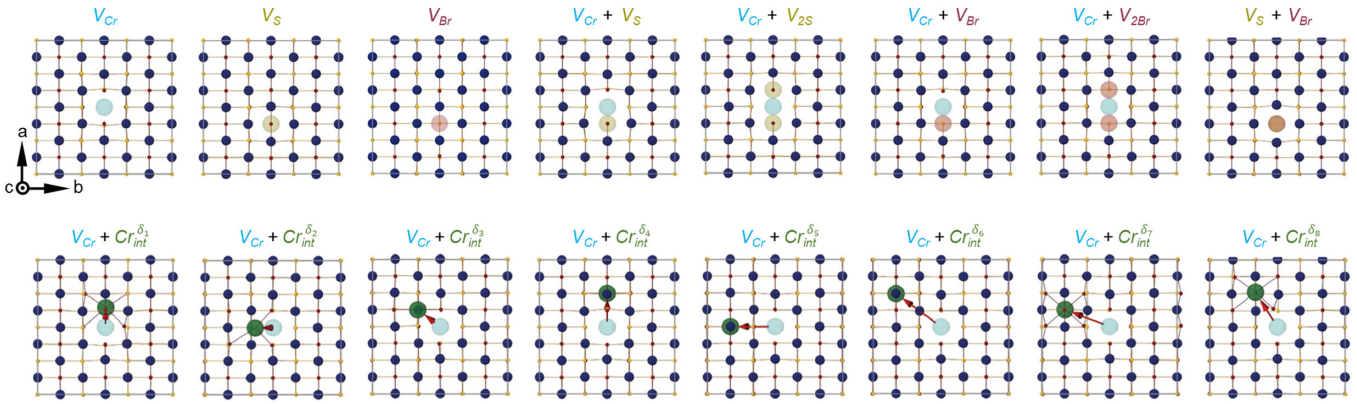


FIG. 6. Library of defects and defect complexes in $2L$ CrSBr. DFT-relaxed crystal structures depicting the top-down view of vacancy defects (V_{Cr}, V_S, and V_{Br}), vacancy defect complexes ($V_{Cr} + V_S$, $V_{Cr} + V_{2S}$, $V_{Cr} + V_{Br}$, $V_{Cr} + V_{2Br}$, and $V_S + V_{Br}$), and vacancy interstitial complexes ($V_{Cr} + Cr_{int}^{\delta n}$).

Consequently, the $2V_{Cr}^{bi}$ shows in-gap impurity states of both spin flavors. Since in this case the inversion symmetry is broken, the spin degeneracy is, however, lifted. Upon close inspection, we see that the breaking of the spin degeneracy due to broken inversion symmetry also holds for the bulk states in both cases.

For Cr interstitial vacancy complexes $V_{Cr} + Cr_{int}^{\delta 1}$ and $V_{Cr} + Cr_{int}^{\delta 2}$, we observe a similar behavior, visible in Fig. 5(c). In the case of $V_{Cr} + Cr_{int}^{\delta 2}$, we find nearly completely flat states, a remarkable result that indicates the highest localization of the corresponding impurity states in real space. In contrast to the simple Cr vacancies, we see that the spin degeneracy of the bulk states is strongly broken. Here, this results from charge transfer from the upper layer toward and into the vdW gap (following the Cr replacement). This strongly enhances the local inversion symmetry breaking. In Supplemental Material [37], we show in detail how this effect is reduced by lowering the impurity density, i.e., by increasing the supercell size. The $V_{Cr} + V_{Br}$ and $V_{Cr} + V_{2Br}$ leave similar footprints in the electronic structure, as seen in Fig. 5(d). However, $V_{Cr} + V_{2Br}$ appears special, as in this case a weakly dispersive impurity band crosses the Fermi level.

We show the relaxed structures of all calculated defects and defect complexes in Fig. 6 and their binding energy densities, electronic symmetry, and potential optical activity in Table I. This emphasizes the fact that most of the defect complexes we have considered should show both occupied and unoccupied in-gap defect states. We can, thus, expect to find single-photon emitters among these defect structures, resulting from interdefect optical excitations or relaxations. Together with their peculiar inherited spin states, this might allow for magnetically controlled single-photon emission. We finally note that the overall flatness of the in-gap defect states indicates a rather high degree of real-space localization of the corresponding defect states and, thus, possibly enhanced Coulomb interaction effects. We could, therefore, expect to find correlated or multireference behavior among the defect complexes we have identified, suggesting that they need to be theoretically described beyond the mean-field level that we have applied here.

TABLE I. Parameters and properties of defects and defect complexes in $2L$ CrSBr. Binding energy densities, symmetry, and potential optical activity based on occupied and unoccupied defect levels.

Defect type	E_{vdW}^{bind} (meV)	$E_{surface}^{bind}$ (meV)	Point group	Optical activity
V_{Cr}	350	350	C_{2v}	Yes
V_S	279	278	C_{2v}	Yes
V_{Br}	161	165	C_{2v}	⋯
$2V_{Cr}^{bi}$	699	⋯	C_{2v}	Yes
$2V_S^{bi}$	557	⋯	C_{2v}	Yes
$2V_{Br}^{bi}$	325	⋯	C_{2v}	⋯
$V_{Cr} + V_{Br}$	300	306	C_S	Yes
$V_{Cr} + V_{2Br}$	282	293	C_{2v}	Yes
$V_{Cr} + V_S$	603	602	C_S	Yes
$V_{Cr} + V_{2S}$	710	707	C_{2v}	Yes
$V_S + V_{Br}$	402	407	C_S	Yes

Defect type	E_{vdW}^{bind} (meV)	$E_{surface}^{bind}$ (meV)	Point group	Optical activity
$V_{Cr} + Cr_{int}^{\delta 1}$	149	171	C_S	Yes
$V_{Cr} + Cr_{int}^{\delta 2}$	105	119	C_S	Yes
$V_{Cr} + Cr_{int}^{\delta 3}$	126	140	C_1	Yes
$V_{Cr} + Cr_{int}^{\delta 4}$	134	155	C_S	Yes
$V_{Cr} + Cr_{int}^{\delta 5}$	167	189	C_S	Yes
$V_{Cr} + Cr_{int}^{\delta 6}$	166	189	C_1	Yes
$V_{Cr} + Cr_{int}^{\delta 7}$	173	189	C_1	Yes
$V_{Cr} + Cr_{int}^{\delta 8}$	146	155	C_1	Yes

IV. CONCLUSION

We have established a defect library in CrSBr by combining atomic resolution STEM, deep learning, and theoretical *ab initio* calculations. Because of its unusual crystal structure, CrSBr exhibits a large set of defects and defect complexes, including single and vertically stacked vacancies, interstitial-vacancy defect complexes, and vacancy defect complexes. The results show that machine learning is effective in assisting the identification of defect types known to be present, particularly in scenarios where materials are beam sensitive and only very low doses can be used to obtain images. The use of deep learning enabled us to detect defect complexes that expand over more than one atom column, features that are otherwise challenging to resolve using conventional image analysis methods. However, by integrating and analyzing multiple images, more subtle features of the atomic arrangement could be uncovered. For CrSBr bilayers, this enhanced visualization showed that structures that appeared at first to be single vacancy defects were, in fact, more complex configurations.

In particular, we detected V_{Cr} defects associated with $\mathrm{Cr}_{\mathrm{int}}$ at specific locations predicted by DFT, and V_{Cr} defects linked with V_{Br} in a pattern explained by the geometric bond configuration within the structure. The interstitial defects are particularly compelling, as our results suggest that they create highly localized electronic states with optical transitions. Furthermore, detecting extended defect lines along the a directions and a power-law distribution of their occurrence suggest correlated growth and provide an important framework to interpret defect-related transport measurements.

Our atomically precise measurement of these CrSBr defects and defect complexes creates an absolutely necessary foundation for further higher-level theoretical investigations of defect-induced electronic, magnetic, and optical properties. Based on our initial mean-field results indicating highly localized real-space defect states, we expect $V_{\mathrm{Cr}} + \mathrm{Cr}_{\mathrm{int}}^{\delta 2}$ and $V_{\mathrm{Cr}} + V_{2\mathrm{Br}}$ to be especially interesting in potentially hosting (strongly) correlated properties.

Moreover, to the best of our knowledge, our work offers the first experimental atomic-scale defect study that is representative for the structural FeOCl type with *Pmmn* space group symmetry. As such, our results in CrSBr are a blueprint for defects such as interstitials and vacancy complexes that are similarly expected in more than 20 predicted compounds [51] such as the family of transition metal oxyhalides (MOX with $M =$ Fe, Cr, V, Ti, Dy, Eu and $X =$ Cl, Br, I) [51,52] and transition metal chalcogenide halides ($M\mathrm{Ch}X$ with Ch = S, Se) similar to CrSBr, like CrSI, DySBr, ErSeI, ErSI, and many more [51].

Looking ahead, this work clarifies how the unique energetic landscapes of Cr atoms in CrSBr create an environment that allows the formation of intriguing localized magnetoelectronic defect states. The defects are expected to exhibit optical properties akin to quantum emitters in other layered materials [1]. The presence of optically active defects is particularly exciting, as CrSBr is known to maintain monolayer properties in bulk form [20,53], so the defects we discussed in bilayers of CrSBr can be straightforwardly extrapolated to the multilayer or bulk system. Indeed, bulk CrSBr has shown optically active defect emission for which the origin is still under debate [24]. Our detailed experimental and theoretical results suggest a plethora of optically active defects in CrSBr. The methodology we have developed to characterize defects in multilayer systems and the properties of defects, particularly related to Cr, motivates future work to pursue atomic-scale modification of CrSBr via focused electron beams [27] for the deliberate generation of defect complexes relevant for quantum technologies.

ACKNOWLEDGMENTS

J. K. and F. M. R. acknowledge funding through the NSF Trailblazer Award No. 2421694 and DOE-BES Award No. DE-SC0025387. The authors acknowledge the MIT SuperCloud and Lincoln Laboratory Supercomputing Center for providing HPC, database, and consultation resources that have contributed to the research results reported in this paper [54]. Synthesis work at Columbia University was supported by the National Science Foundation through the Columbia University Materials Research Science and Engineering Center (MRSEC) on Precision-Assembled Quantum Materials DMR-2011738. Z. S. was supported by the ERC-CZ program (Project No. LL2101) from Ministry of Education Youth and Sports (MEYS) and by the project Advanced Functional Nanorobots (Reg. No. CZ.02.1.01/0.0/0.0/15_003/0000444 financed by the EFRR). The Center for Visualizing Catalytic Processes (VISION) is funded by the Danish National Research Foundation (DNRF146). M. R. acknowledges support from the Vidi ENW research programme of the Dutch Research Council (NWO) under the Grant https://doi.org/10.61686/YDRHT18202 with file number VI.Vidi.233.077. The computations were performed at the Dutch National Supercomputer Snellius under Project No. EINF-4184. This work was carried out in part through the use of MIT.nano's facilities. We thank Matthias Florian for fruitful discussions. We acknowledge referee 2 for the valuable suggestion that led us to extend the statistical analysis of vacancy defect lines.

J. K. conceptualized and supervised the project and together with M. W. designed the experiments. X. R., D. C., Z. S., and K. M. synthesized bulk crystals of CrSBr. J. K. prepared STEM samples. J. K. and A. P. collected STEM data. M. W. developed the machine learning work flow. S. G. and M. R. provided *ab initio* DFT calculations. J. S., S. H., and F. M. R. discussed the results. The manuscript was written by M. W. and J. K. with input from all coauthors.

DATA AVAILABILITY

The data that support the findings of this article are openly available [44].

APPENDIX A: CRYSTAL GROWTH

Two separate sources of crystals were used and gave similar results. These crystals were fabricated using chemical vapor transport as described in Refs. [17,27].

APPENDIX B: SAMPLE FABRICATION

Samples were fabricated by mechanical exfoliation of CrSBr onto SiO_2/Si substrates. Sample thickness was verified by atomic force microscopy, optical phase contrast, and Raman spectroscopy. The samples were then transferred to S/TEM grids using dry polymer assisted transfer. No water was used for the transfer process to avoid additional surface damage due to hydrolysis [28]. For additional information, see Supplemental Material [37].

APPENDIX C: SCANNING TRANSMISSION ELECTRON MICROSCOPY

The STEM imaging was conducted on a probe-corrected Thermo Fisher Scientific Themis Z G3. The microscope was operated at a 200 keV acceleration energy, a beam current of 35 pA and a semiconvergence angle of 19 mrad. This provided an aberration-corrected sub-angstrom probe size (typically, 80 pm) allowing for atomic resolution. The images were all captured at 1024×1024 pixels with a pixel size of 7.8 pm. We used a short pixel dwell time of 500 ns/px corresponding to a single image dose of 9×10^5 e^-/nm^2. Because of the structural sensitivity of bilayer CrSBr under the electron beam, we optimized image acquisition. We collected and averaged a series of ten images using rigid registration [45] with a total image dose of 9×10^6 e^-/nm^2. For each image series, it was necessary to adopt a specific acquisition strategy: We set a very low magnification to reduce dose, moved to a new and unexposed area, and then immediately started a blind image acquisition at higher magnification. This approach ensured that the material was not exposed to the electron beam before data collection. As a result, most images are out of focus considering height variations across the sample, but after postselection a small fraction of images remained for our deep learning analysis.

APPENDIX D: IMAGE SIMULATIONS

HAADF-STEM image simulations were conducted with microscope parameters that matched the experimental conditions. The HAADF-STEM simulations used in the illustrations and in the datasets for training were constructed using abTEM [55], a PYTHON package for electron microscopy simulations. The simulations were accelerated using the plane wave reciprocal space interpolated scattering matrix (PRISM) [56] algorithm, since STEM simulations are typically computationally expensive. During simulations of the training data, several microscope aberrations were applied.

For our comparison to the class averages of the defects, we likewise used PRISM with detector collection angles of 78–200 mrad and a semiconvergence angle of 19 mrad and an interpolation factor of 1, but without any aberrations. We smoothed simulated images with a Gaussian full width at half maximum (FWHM) of 80 pm to match the experimental probe size and to account for thermal vibrations. Furthermore, the images were constructed by taking the average STEM-HAADF simulation between the two different sites within the unit cell where the defect could occur. The resulting line profiles were created by summing the intensity over the FWHM of the atoms, similarly done for both simulated and experimental data.

APPENDIX E: MACHINE LEARNING FRAMEWORK

In this work, we utilized a UNet++ [36] architecture with a depth of 5 to analyze HAADF-STEM images. We compared the UNet++ network to seven other network architectures and found that for our use cases it consistently outperformed them, including the UNet when tasked to find the position of atoms (see Supplemental Material [37]). The architecture is a derivative of the popular UNet [43] and provides additional pathways and an increased amount of blocks at several scales resulting in a more reliable information transfer. The training dataset was constructed using the PYTHON package abTEM [55] and ASE [57] to simulate images of $2L$ CrSBr with randomly introduced defects. The complete overview of the simulations and the training process is shown in Supplemental Material [37], and the corresponding code is available [44].

APPENDIX F: *Ab initio* CALCULATIONS

For structure optimization and total energy calculations, we used the Vienna *Ab Initio* Simulation Package (VASP) [58,59] utilizing projector augmented plane waves [60,61] as the basis. To approximately address electronic correlations, we applied the rotationally invariant GGA + U approach with $U = 2.5$ eV and $J = 0.4$ eV (constrained random phase approximation values for single-layer CrSBr in an effective dielectric environment of $\varepsilon_{\mathrm{env}} \approx 8$ [62]) acting within the Cr d orbitals. The Perdew-Burke-Ernzerhof [63] form of the GGA exchange-correlation potentials was used. For the simulation of defects in $2L$ structures, we utilized $(4 \times 3 \times 2)$ supercells with a vacuum of 30 Å, $2 \times 2 \times 1$ Monkhorst-Pack k grids, and a plane-wave cutoff energy of 500 eV. The atomic positions are fully relaxed until all Hellmann-Feynman forces acting on each atom are reduced to (or below) 0.01 eV/Å.

[1] A. R.-P. Montblanch, M. Barbone, I. Aharonovich, M. Atatüre, and A. C. Ferrari, *Layered materials as a platform for quantum technologies*, Nat. Nanotechnol. **18**, 555 (2023).

[2] Z. Lin *et al.*, *Defect engineering of two-dimensional transition metal dichalcogenides*, 2D Mater. **3**, 022002 (2016).

[3] M. Atatüre, D. Englund, N. Vamivakas, S.-Y. Lee, and J. Wrachtrup, *Material platforms for spin-based photonic quantum technologies*, Nat. Rev. Mater. **3**, 38 (2018).

[4] D. Voiry *et al.*, *Enhanced catalytic activity in strained chemically exfoliated* WS_2 *nanosheets for hydrogen evolution*, Nat. Mater. **12**, 850 (2013).

[5] J. Kotakoski, A. V. Krasheninnikov, U. Kaiser, and J. C. Meyer, *From point defects in graphene to two-dimensional amorphous carbon*, Phys. Rev. Lett. **106**, 105505 (2011).

[6] H.-P. Komsa, J. Kotakoski, S. Kurasch, O. Lehtinen, U. Kaiser, and A. V. Krasheninnikov, *Two-dimensional transition metal dichalcogenides under electron irradiation: Defect production and doping*, Phys. Rev. Lett. **109**, 035503 (2012).

[7] W. Zhou *et al.*, *Intrinsic structural defects in monolayer molybdenum disulfide*, Nano Lett. **13**, 2615 (2013).

[8] D. O. Dumcenco, H. Kobayashi, Z. Liu, Y.-S. Huang, and K. Suenaga, *Visualization and quantification of transition metal atomic mixing in* $Mo_{1-x}W_xS_2$ *single layers*, Nat. Commun. **4**, 1351 (2013).

[9] J. C. Meyer, A. Chuvilin, G. Algara-Siller, J. Biskupek, and U. Kaiser, *Selective sputtering and atomic resolution imaging of atomically thin boron nitride membranes*, Nano Lett. **9**, 2683 (2009).

[10] C. Gong *et al.*, *Discovery of intrinsic ferromagnetism in two-dimensional van der Waals crystals*, Nature (London) **546**, 265 (2017).

[11] D. Shcherbakov *et al.*, *Raman spectroscopy, photocatalytic degradation, and stabilization of atomically thin chromium tri-iodide*, Nano Lett. **18**, 4214 (2018).

[12] Y. Deng *et al.*, *Gate-tunable room-temperature ferromagnetism in two-dimensional* Fe_3GeTe_2, Nature (London) **563**, 94 (2018).

[13] M. Bonilla *et al.*, *Strong room-temperature ferromagnetism in* VSe_2 *monolayers on van der Waals substrates*, Nat. Nanotechnol. **13**, 289 (2018).

[14] Y. Liu *et al.*, *The environmental stability characterization of exfoliated few-layer* $CrXTe_3$ *(*X = Si, Ge*) nanosheets*, Appl. Surf. Sci. **511**, 145452 (2020).

[15] H. Katscher and H. Hahn, *Über Chalkogenidhalogenide des dreiwertigen Chroms*, Naturwissenschaften **53**, 361 (1966).

[16] O. Göser, W. Paul, and H. Kahle, *Magnetic properties of* CrSBr, J. Magn. Magn. Mater. **92**, 129 (1990).

[17] E. J. Telford *et al.*, *Layered antiferromagnetism induces large negative magnetoresistance in the van der Waals semiconductor* CrSBr, Adv. Mater. **32**, 2003240 (2020).

[18] M. D. Watson *et al.*, *Giant exchange splitting in the electronic structure of A-type 2D antiferromagnet* CrSBr, npj 2D Mater. Appl. **8**, 54 (2024).

[19] M. Bianchi *et al.*, *Paramagnetic electronic structure of* CrSBr*: Comparison between ab initio GW theory and angle-resolved photoemission spectroscopy*, Phys. Rev. B **107**, 235107 (2023).

[20] J. Klein *et al.*, *The bulk van der Waals layered magnet* CrSBr *is a quasi-1D material*, ACS Nano **17**, 5316 (2023).

[21] K. Lee *et al.*, *Magnetic order and symmetry in the 2D semiconductor* CrSBr, Nano Lett. **21**, 3511 (2021).

[22] F. Wu *et al.*, *Quasi-1D electronic transport in a 2D magnetic semiconductor*, Adv. Mater. **34**, 2109759 (2022).

[23] E. J. Telford *et al.*, *Coupling between magnetic order and charge transport in a two-dimensional magnetic semiconductor*, Nat. Mater. **21**, 754 (2022).

[24] J. Klein *et al.*, *Sensing the local magnetic environment through optically active defects in a layered magnetic semiconductor*, ACS Nano **17**, 288 (2022).

[25] F. Long *et al.*, *Ferromagnetic interlayer coupling in* CrSBr *crystals irradiated by ions*, Nano Lett. **23**, 8468 (2023).

[26] M. A. Tschudin *et al.*, *Imaging nanomagnetism and magnetic phase transitions in atomically thin* CrSBr, Nat. Commun. **15**, 6005 (2024).

[27] J. Klein *et al.*, *Control of structure and spin texture in the van der Waals layered magnet* CrSBr, Nat. Commun. **13**, 5420 (2022).

[28] K. Torres *et al.*, *Probing defects and spin-phonon coupling in* CrSBr *via resonant Raman scattering*, Adv. Funct. Mater. **33**, 2211366 (2023).

[29] M. Ziatdinov *et al.*, *Deep learning of atomically resolved scanning transmission electron microscopy images: Chemical identification and tracking local transformations*, ACS Nano **11**, 12742 (2017).

[30] J. Madsen *et al.*, *A deep learning approach to identify local structures in atomic-resolution transmission electron microscopy images*, Adv. Theory Simul. **1**, 1800037 (2018).

[31] A. Maksov *et al.*, *Deep learning analysis of defect and phase evolution during electron beam-induced transformations in* WS_2, npj Comput. Mater. **5**, 12 (2019).

[32] C.-H. Lee *et al.*, *Deep learning enabled strain mapping of single-atom defects in two-dimensional transition metal dichalcogenides with sub-picometer precision*, Nano Lett. **20**, 3369 (2020).

[33] S. V. Kalinin *et al.*, *Machine learning in scanning transmission electron microscopy*, Nat. Rev. Methods Primers **2**, 11 (2022).

[34] J. Beck, *Über Chalkogenidhalogenide des Chroms Synthese, Kristallstruktur und Magnetismus von Chromsulfidbromid,* CrSBr, Z. Anorg. Allg. Chem. **585**, 157 (1990).

[35] A. Sagua *et al.*, *Lithium intercalation in* FeOCl *revisited*, Int. J. Inorg. Mater. **3**, 293 (2001).

[36] Z. Zhou, M. M. Rahman Siddiquee, N. Tajbakhsh, and J. Liang, *UNet++: A Nested U-Net Architecture for Medical Image Segmentation* (Springer, New York, 2018), pp. 3–11.

[37] See Supplemental Material at http://link.aps.org/supplemental/10.1103/PhysRevX.15.021080 for a detailed description of sample preparation and microscopic structural stability, the formation of Cr interstitial defects under electron beam irradiation, the machine learning work flow, experimental images of defect complexes and extended line defects, and theoretical calculations of vacancies, surface and van der Waals interstitial defects, defect complexes, and line defects.

[38] Eevee, Perlin noise, https://eev.ee/blog/2016/05/29/perlin-noise/.

[39] Y.-C. Lin *et al.*, *Graphene annealing: How clean can it be?*, Nano Lett. **12**, 414 (2011).
[40] O. Dyck, A. R. Lupini, P. D. Rack, J. Fowlkes, and S. Jesse, *Controlling hydrocarbon transport and electron beam induced deposition on single layer graphene: Toward atomic scale synthesis in the scanning transmission electron microscope*, Nano Sel. **3**, 643 (2021).
[41] H. Yang *et al.*, *Simultaneous atomic-resolution electron ptychography and Z-contrast imaging of light and heavy elements in complex nanostructures*, Nat. Commun. **7**, 12532 (2016).
[42] M. Ziatdinov *et al.*, *Building and exploring libraries of atomic defects in graphene: Scanning transmission electron and scanning tunneling microscopy study*, Sci. Adv. **5**, aaw8989 (2019).
[43] O. Ronneberger, P. Fischer, and T. Brox, *U-Net: Convolutional networks for biomedical image segmentation*, arXiv:1505.04597.
[44] M. Weile and J. Klein, *2D defect detection*, https://github.com/MadsAW/2d-defect-detection.
[45] B. H. Savitzky *et al.*, *Image registration of low signal-to-noise cryo-STEM data*, Ultramicroscopy **191**, 56 (2018).
[46] O. L. Krivanek *et al.*, *Atom-by-atom structural and chemical analysis by annular dark-field electron microscopy*, Nature (London) **464**, 571 (2010).
[47] Y. Cheng and T. Walz, *The advent of near-atomic resolution in single-particle electron microscopy*, Annu. Rev. Biochem. **78**, 723 (2009).
[48] F. F. Krause *et al.*, *Comparison of intensity and absolute contrast of simulated and experimental high-resolution transmission electron microscopy images for different multislice simulation methods*, Ultramicroscopy **134**, 94 (2013).
[49] K. MacArthur *et al.*, *Probe integrated scattering cross sections in the analysis of atomic resolution HAADF STEM images*, Ultramicroscopy **133**, 109 (2013).
[50] N. P. Wilson *et al.*, *Interlayer electronic coupling on demand in a 2D magnetic semiconductor*, Nat. Mater. **20**, 1657 (2021).
[51] N. Mounet *et al.*, *Two-dimensional materials from high-throughput computational exfoliation of experimentally known compounds*, Nat. Nanotechnol. **13**, 246 (2018).
[52] M. Armand, L. Coic, P. Palvadeau, and J. Rouxel, *The M-0-X transition metal oxyhalides: A new class of lamellar cathode material*, J. Power Sources **3**, 137 (1978).
[53] J. Klein and F. M. Ross, *Materials beyond monolayers: The magnetic quasi-1D semiconductor* CrSBr, J. Mater. Res. **39**, 3045 (2024).
[54] A. Reuther *et al.*, *Interactive supercomputing on 40,000 cores for machine learning and data analysis*, in *Proceedings of the 2018 IEEE High Performance Extreme Computing Conference (HPEC)* (IEEE, New York, 2018), https://ieeexplore.ieee.org/document/8547629.
[55] J. Madsen and T. Susi, *The abtem code: Transmission electron microscopy from first principles*, Open Res. Eur. **1**, 24 (2021).
[56] C. Ophus, *A fast image simulation algorithm for scanning transmission electron microscopy*, Adv. Struct. Chem. Imaging **3**, 13 (2017).
[57] A. Hjorth Larsen *et al.*, *The atomic simulation environment—A* PYTHON *library for working with atoms*, J. Phys. Condens. Matter **29**, 273002 (2017).
[58] G. Kresse and J. Furthmüller, *Efficiency of ab-initio total energy calculations for metals and semiconductors using a plane-wave basis set*, Comput. Mater. Sci. **6**, 15 (1996).
[59] G. Kresse and J. Furthmüller, *Efficient iterative schemes for ab initio total-energy calculations using a plane-wave basis set*, Phys. Rev. B **54**, 11169 (1996).
[60] P. E. Blöchl, *Projector augmented-wave method*, Phys. Rev. B **50**, 17953 (1994).
[61] G. Kresse and D. Joubert, *From ultrasoft pseudopotentials to the projector augmented-wave method*, Phys. Rev. B **59**, 1758 (1999).
[62] A. N. Rudenko, M. Rösner, and M. I. Katsnelson, *Dielectric tunability of magnetic properties in orthorhombic ferromagnetic monolayer* CrSBr, npj Comput. Mater. **9**, 83 (2023).
[63] J. P. Perdew, K. Burke, and M. Ernzerhof, *Generalized gradient approximation made simple*, Phys. Rev. Lett. **77**, 3865 (1996).